Applied Catalysis B: Environmental 238 (2018) 198–211

Contents lists available at ScienceDirect

Applied Catalysis B: Environmental

journal homepage: www.elsevier.com/locate/apcatb

Connecting structural, optical, and electronic properties and photocatalytic activity of Ag_3PO_4:Mo complemented by DFT calculations

Aline Barrios Trench[a], Thales Rafael Machado[a], Amanda Fernandes Gouveia[a], Marcelo Assis[a], Letícia Guerreiro da Trindade[b], Clayane Santos[a], Andre Perrin[c], Christiane Perrin[c], Mónica Oliva[d], Juan Andrés[d,*], Elson Longo[a]

[a] CDMF, Universidade Federal de Sao Carlos, P.O. Box 676, Sao Carlos, SP, 13565-905, Brazil
[b] Institute of Chemistry, UFRGS, P.O. Box 15003, Porto Alegre, RS, 91501-970, Brazil
[c] University of Rennes 1, Campus de Beaulieu, av. Général Leclerc, F-35042, Rennes-Cedex, France
[d] Department of Analytical and Physical Chemistry, University Jaume I, Castellón, 12071, Spain

ARTICLE INFO

Keywords:
Ag3PO4:Mo microcrystals
Photocatalytic activity
DFT calculations

ABSTRACT

The present join experimental and theoretical work provides in-depth understanding on the relationship among structural, optical, and electronic properties and photocatalytic activity of Ag_3PO_4:Mo microcrystals. We prepared Ag_3PO_4 and (Mo-doped) Ag_3PO_4:Mo microcrystals using the chemical precipitation method. The as-synthetized samples have been characterized by X-ray diffraction (XRD), X-ray photoelectron spectroscopy, transmission electron microscopy, high angle annular dark field scanning transmission electron microscopy (HAADF-STEM), energy-dispersive X-ray spectroscopy (EDS) techniques, and photoluminescence (PL) emission. Density functional theory calculations have been performed to complement the experimental results and understand the physical phenomena taking place in the structure, electronic and optical properties involved in the Mo doping process on the Ag_3PO_4, and consequently the photocatalytic performances of these new materials. XRD analysis showed that at a doping level below 2% the samples did not present any secondary phases, demonstrating that the Mo cations have been actually incorporated in the Ag_3PO_4 structure. Moreover, HAADF-STEM and EDS mapping showed that the samples were homogeneous, especially with respect to the Mo cations, and showed no signs of segregation. The E_{gap} value and PL measurements indicated that the doping process caused structural defects in the Ag_3PO_4 structure. The photocatalytic activity of both the pure and Mo-doped materials was tested for the degradation of Rhodamine B under visible light irradiation. The results demonstrated that the sample of Ag_3PO_4:Mo with 0.5% Mo had a faster degradation rate, approximately 92% after 5 min of irradiation, while the degradation rate of the pure sample was only 46% during the same time.

1. Introduction

Semiconductor silver orthophosphate, Ag_3PO_4, has received considerable attention owing to its high performance in photocatalytic applications [1–3], where it exhibits extremely high photooxidative capabilities for O_2 evolution from water and organic dye decomposition under visible-light irradiation. Ag_3PO_4 has also present bacteriostatic [4] and antibacterial [5] properties. However, the practical uses of Ag_3PO_4 are limited by its photocorrosion, because its conduction band (CB) potential is higher than the reduced potential of H_2O/H_2 [6]. This limitation has prompted significant research efforts to develop chemically modified Ag_3PO_4, and has been reported in detail in a recent review (see X. Chen et al. [6] and references therein). Considerable efforts were made to improve this material by (i) controlling the morphology, including the use of different precursors, pH, organic additives, templates, and facet-controlled growth, and (ii) material modification, by metal deposition, cation or anion doping, or coupling with another semiconductor.

Song et al. [7] reported the stability and high photocatalytic activity of the CeO_2/Ag_3PO_4 composite under visible light irradiation. Yang et al. [8] synthetize an efficient Ag_3PO_4/g-C_3N_4 composite material as photocatalyst for oxygen production and pollutant degradation by using electrostatically driven assembly and ion-exchange processes, while Tang et al. [9] developed a high efficiency visible-light-driven Ag_3PO_4/Ag_2MoO_4 composite material with excellent photocatalytic activity in the degradation of typical dyes (rhodamine B – RhB, methyl

* Corresponding author.
E-mail address: andres@qfa.uji.es (J. Andrés).

https://doi.org/10.1016/j.apcatb.2018.07.019
Received 6 April 2018; Received in revised form 5 July 2018; Accepted 8 July 2018
Available online 10 July 2018
0926-3373/

orange – MO and methylene blue – MB). In a recent paper, Cao et al. [10] reported on visible-light-driven β-Ag_2MoO_4/Ag_3PO_4 composites with enhanced photocatalytic activity where they first precipitated a very small amount of β-Ag_2MoO_4 followed by the precipitation of Ag_3PO_4. In this study, we used a different approach by substituting some P(V) cations in the Ag_3PO_4 network with Mo(VI) at a predetermined doping concentration to create intermediate levels in the band gap. Depending on the synthesis conditions, Ag_3PO_4 microcrystals present various sizes and shapes; for instance, Cao et al. [10] and Botelho et al. [11] reported round particles in the 130–400 nm diameter range, while Botelho et al. [12], observed well-defined polyhedra, in a sample processed in a microwave hydrothermal assisted system from a silver diamine complex.

Doping involving the intentional incorporation of specific cations into host lattices to generate materials with desirable functions is a widely applied technological process for controlling and tuning the electronic properties of semiconductors. Introducing small amounts of foreign elements (usually transition metals) into the conventional metal oxide matrix is a strategy frequently used to manipulate the band gap [13–16]. The dopants may generate new energy levels between the valence band (VB) and CB of the metal oxide resulting in a reduced minimum light absorption energy gap of the host lattice [7]. Very recently, Hussien and Yahia [17] have analyzed the performance of nanostructured molybdenum-doped Ag_3PO_4 as visible photocatalyst. The synthesis procedure of their "doped" samples suggests that they precipitated first β-Ag_2MoO_4, then it is expected that they obtained in fact a composite material (not doped, in contrast to our one) similar to that of Cao et al. [10].

Our group is engaged in research projects devoted to the study of the structural, morphological, optical, and photocatalytic properties of Ag_3PO_4 microcrystals using a combination of theoretical calculations and experimental techniques [11,12]. As an extension of our research, we have developed a new, innovative method for the synthesis of Ag_3PO_4:Mo doped powders, clearly different from the recently reported preparation of Ag_3PO_4/β-Ag_2MoO_4 composites [10], and reported it here. To gain further insight, we performed density functional theory (DFT) calculations to complement the experimental results and understand the physical phenomena associated with the structure, electronic and optical properties involved in the Mo doping process of Ag_3PO_4, and consequently the photocatalytic performances of these new materials.

2. Experimental procedures

2.1. Synthesis of pure- and Mo-doped Ag_3PO_4 microcrystals

Both Ag_3PO_4 and Ag_3PO_4:Mo microcrystals were obtained by chemical precipitation (CP) method in aqueous media at room temperature. The precursor salts employed in this synthesis were $(NH_4)_2HPO_4$ (0.001 M, 50 mL) (98.6%, J.T. Baker) and $AgNO_3$ (0.003 M, 50 mL) (99.8%,Vetec). The dopant source was $Na_2MoO_4{\cdot}2H_2O$ (Vetec). Two solutions were prepared: (i) $(NH_4)_2HPO_4$ diluted in 50 mL deionized water at 30 °C under stirring for complete dissolution of the salt and (ii) $AgNO_3$ diluted in 50 mL deionized water at 30 °C under stirring. After the complete dissolution of (i), the dopant was immediately added in molar proportions of x = 0.000, 0.005, 0.01, 0.02, 0.04, and 0.08 with respect to the $Ag_3(P_{1-x}Mo_x)O_4$ system. Subsequently, solution (ii) was added to solutions (i) and stirred for 10 min to obtain yellow precipitates. The resulting materials were centrifuged five times with deionized water to remove the soluble salts. Afterward, the precipitates were dried in an oven at 60 °C for 1 day, so that no changes occur in their properties. Henceforth, these samples will be referred to as pure Ag_3PO_4, Ag_3PO_4:Mo 0.5%, Ag_3PO_4:Mo 1%, Ag_3PO_4:Mo 2%, Ag_3PO_4:Mo 4%, and Ag_3PO_4:Mo 8%.

2.2. Characterization

The microcrystalline powders were characterized using X-ray diffraction (XRD) with a D/Max-2500PC diffractometer (Rigaku, Japan) involving CuK α radiation (λ = 1.54056 Å) in the 15–100° 2θ range at a step scan rate and step size values of 1°/min and 0.02°, respectively. Rietveld refinements were performed using the general structure analysis system (GSAS) software package with the EXPGUI graphical interface. The theoretical diffraction pattern was retrieved from the *Inorganic Crystal Structure Database* (ICSD) No. 14000, which is based on the body-centered cubic structure with space group $P\,\bar{4}3\,n$. Micro-Raman spectroscopy was carried out using an iHR550 spectrometer (Horiba Jobin-Yvon, Japan) coupled to a charge-coupled device (CCD) detector and an argon-ion laser (MellesGriot, USA) operating at 514.5 nm with a maximum power of 200 mW. The spectra were measured in the 100–1100 cm^{-1} range. X-ray photoelectron spectroscopy (XPS) analyses were performed on a Scienta Omicron ESCA + spectrometer (Germany) using monochromatic Al Kα (1486.7 eV). Peak deconvolution was performed using a 70% Gaussian and 30% Lorentzian line shape with a Shirley nonlinear sigmoid-type baseline. The binding energies of all elements were calibrated by referencing to the C 1s peak at 284.8 eV. Morphologies were analyzed using field emission gun scanning electron microscopy (FEG-SEM) on an FEI instrument (Model Inspect F50) operating at 10 kV. The BET surface area (S_{BET}) and particle sizes of the samples was studied using N_2 adsorption and desorption isotherms measured at 77 K on a Micromeritics ASAP 2420 A (USA) surface area and porosimetry analyzer. Prior to the N_2 adsorption measurement, the samples were degassed at 200 °C under vacuum for 4 h. The S_{BET} of the samples was calculated using the Brunauer-Emmett-Teller (BET) method in the relative pressure (P/P_0) range of 0.05–0.16. Transmission electron microscopy (TEM) and high-resolution TEM (HR-TEM), as well as energy-dispersive X-ray spectroscopy (EDS) analysis, were performed using a FEI Tecnai F20 (Netherlands) microscope operating at 200 kV. High angle annular dark-field (HAADF) images and EDS mapping were recorded in the scanning transmission electron microscopy (STEM) mode. Ultraviolet-visible (UV–vis) absorption spectra were recorded using a Varian spectrophotometer model Cary 5 G (USA) in the diffuse reflection mode. Photoluminescence (PL) spectra were measured using a Monospec 27 monochromator (Thermal, Jarrel Ash, USA) coupled to a R446 photomultiplier (Hamamatsu Photonics, Japan). A krypton ion laser (Coherent Innova, 200 K, USA) (λ = 350 nm) was used as the excitation source. The incident laser beam power on the sample was maintained at 15 mW.

2.3. Photocatalytic activity

The photocatalytic activity of the pure Ag_3PO_4 and Ag_3PO_4:Mo samples was tested for the degradation of Rhodamine B (RhB) (Aldrich 95%) in aqueous solutions under visible light irradiation. We dispersed Ag_3PO_4:Mo (50 mg) with different doping levels in a RhB solution (50 mL 1×10^{-5} mol L^{-1}) in a beaker placed in an ultrasonic bath (Branson, model 1510; frequency 42 kHz) for 30 min. This solution was maintained in the dark, under stirring for 30 min to allow the adsorption-desorption equilibrium of the dye on the catalysts. We called the collection time of the first aliquot time 0. Subsequently, these solutions were illuminated by six lamps (Philips TL-D, 15 W) in a photocatalytic system maintained at 20 °C in a thermostatic bath with vigorous stirring. Aliquots were collected at fixed time intervals (0, 5, 10, and 15 min) and centrifuged to obtain the liquid phase alone. Variations in the absorption band maximum at λ = 553 nm (RhB) were measured by performing UV–vis absorption spectroscopy measurements of the solution on a V-660 spectrophotometer (JASCO). To propose the photocatalytic mechanism, we performed tests by adding appropriate reactive species collectors; we used 0.067 g of benzoquinone (BQ) (Alfa Aesar), 0.088 g of ammonium oxalate (AO) (Alfa Aesar), 0.0589 mL of

tert-butyl alcohol (TBA) (Alfa Aesar) and 0.047 mL of isopropyl alcohol (IPA) (Alfa Aesar) as scavengers. The total organic carbon (TOC) assays were tested by using a SUEZ-GE Sievers Innovox (France) analyzer.

2.4. Computational methods

The theoretical calculations for the Ag_3PO_4 and Ag_3PO_4:Mo structures were performed using the CRYSTAL14 software package [18,19]. Moreover, DFT calculations at the B3LYP hybrid functional level were performed [20,21]. The diagonalization of the Fock matrix was performed using an adequate number of *k*-point grids in the reciprocal-space. The thresholds controlling the accuracy of the calculations of the Coulomb and exchange integrals were set to 1×10^{-8} and 1×10^{-14}, respectively, and the percentage of Fock/Kohn-Sham matrix mixing was set to 40. The basis sets to describe the atomic centers of Ag, P, O, and Mo were described by PS-311d31 G, 85-21d1G, 6-31d1, and PS-311(d31)G respectively, where PS stands for Hay and Wadt's non-relativistic small core pseudopotential. These were obtained from the CRYSTAL web site [22]. The lattice parameters and internal atomic coordinates of the bulk Ag_3PO_4 were fully optimized until all force components were less than 10^{-6}eV $Å^{-2}$. Two $2 \times 2 \times 2$ supercell periodic models for pure Ag_3PO_4 and Ag_3PO_4:Mo were built using the optimized lattice parameters to accurately describe the structural and electronic properties derived from the experimental synthesis. In one supercell, there were 16 Ag_3PO_4 units, where one P(V) cation was replaced by one Mo(VI) cation to build the Ag_3PO_4:Mo model. Therefore, to ensure the electroneutrality of the system, it was necessary to create a load balance, by generating an Ag^+ vacancy near the Mo(VI) cation. Our Ag_3PO_4:Mo model contains 6.25% Mo in the structure. Unfortunately, obtaining lower percentages of Mo doping would require a larger supercell model and the computational cost is prohibitive.

The energy of formation (ΔE_f) of Ag_3PO_4 and Ag_3PO_4:Mo 6.5% is calculated by subtracting the sum of the energies ($wE_{Ag} + xE_P + yE_O + zE_{Mo}$) of pure constituent elements in their stable crystal structures from the total energy (E_f) by using the following formula [23,24]:

$$\Delta E_f = \frac{E_f - (wE_{Ag} + xE_P + yE_O + zE_{Mo})}{N \times V} \quad (1)$$

where E_f is the total energy, E_{Ag}, E_P, E_O and E_{Mo} denotes the total energy per atom of the pure element Ag, P, O and Mo with w, x, y, z being the number of Ag, P, O and Mo atoms in the cell, N is the sum of the elements ($N = w + x + y + z$) and V is the volume of the model. The calculated total energy, formation energy and the individual energies of the constituent atoms are presented in Table SI-1. The band structure and density of states (DOS) of the models were constructed along the appropriate high-symmetry directions of the corresponding irreducible Brillouin zone.

3. Results and discussion

3.1. XRD analysis

The first crystallographic study of the Ag_3PO_4 microcrystals using single crystal XRD was performed in 1936 by L. Helmholtz, who determined its crystal structure [25]. It is known that Ag_3PO_4 crystallizes in a cubic structure, with the $P\bar{4}3n$ space group, based on a body-centered cubic stacking of isolated regular $[PO_4]$ tetrahedra. These tetrahedra are surrounded by 12 Ag^+ cations located in tetrahedral oxygen sites. Each oxygen anion of the $[PO_4]$ coordination cluster is shared by three $[AgO_4]$ tetrahedral coordination clusters. The Ag^+ cations are located at fully occupied 6*d* sites of -4 symmetry [25,26]. Furthermore, the Ag_3PO_4 structure was re-examined and the position of the Ag^+ cation was split (at 0.15 Å from each other) at the 12*h* site of the twofold symmetry with half occupancy [27,28]. Consequently the $[AgO_4]$ tetrahedra are distorted (*d* Ag–O: 2.357(1) Å × 2 and 2.404(2) Å × 2 [28]).

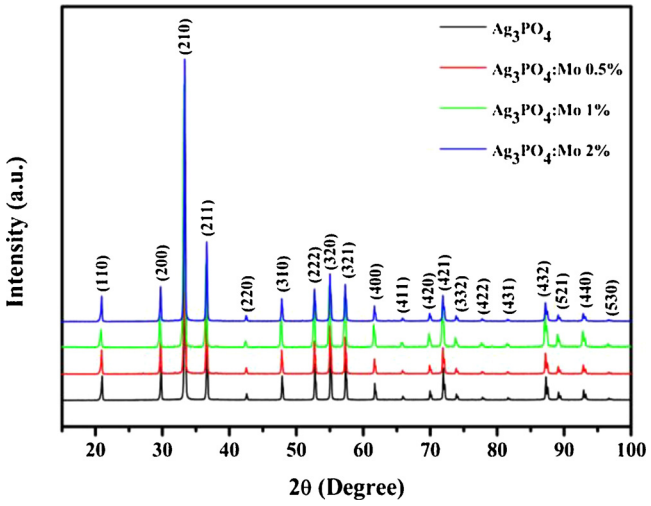

Fig. 1. XRD patterns of Ag_3PO_4, Ag_3PO_4:Mo 0.5%, Ag_3PO_4:Mo 1%, and Ag_3PO_4:Mo 2%.

XRD was employed to obtain the crystal structure and phase composition of Ag_3PO_4 as well as the long-range structural effects of Mo doping on the Ag_3PO_4 structure. Fig. 1(a) shows the XRD patterns obtained for pure Ag_3PO_4 and Ag_3PO_4:Mo 0.5, 1, and 2% samples. The diffraction peaks of all the samples were fully indexed to the cubic structure of Ag_3PO_4, and were all in perfect agreement with the data reported in ICSD No. 14000 [26] and No. 1530 [27]. Moreover, the narrow profiles of the diffraction peaks were related to a high degree of long-range structural ordering. No secondary phase was detected at these doping levels, suggesting that Mo was incorporated into the Ag_3PO_4 structure. By contrast, above the 2% limit, a secondary phase appeared that was clearly related to the presence of β-Ag_2MoO_4, as demonstrated by the XRD patterns of Ag_3PO_4:Mo 4 and 8% samples (see Supporting Information, Fig. SI-1). Because of the formation of secondary phases in the Ag_3PO_4:Mo 4 and 8% samples, no further analyses, such as Rietveld and Raman, were performed.

The structural behavior of the Ag_3PO_4 and Ag_3PO_4:Mo samples was also evaluated by Rietveld analysis. The plots in Fig. SI-2 (Supporting Information) are in agreement with the XRD patterns presented in Fig. 1(a), and the statistic fitting parameters (R_{wp}, R_p, R_{Bragg}, and χ^2) listed in Table 1 revealed an acceptable agreement between the calculated and observed XRD. The values of the unit cell parameters for all samples were calculated using the refinements and are listed in Table 1.

It should be noted that, at this level, the doping only slightly affects the unit-cell constants: the obtained unit-cell constants were 6.01514(2), 6.01582(2), 6.01614(3), and 6.01798(4) Å for pure Ag_3PO_4 and the 0.5, 1, and 2% Mo-doped samples, respectively. The slight increase in unit-cell volume is related to the larger volume of the $[MoO_4]\cdot$ tetrahedron compared to the $[PO_4]$ one, confirming the actual incorporation of Mo into the Ag_3PO_4 lattice. This feature was also proved by the theoretical results, which confirmed that the length of the metal–oxygen bonds was larger in the $[MoO_4]\cdot$clusters (Mo − O = 1.789 Å in average) than in the $[PO_4]$ clusters (P − O = 1.577 Å). The (·) symbol in the $[MoO_4]\cdot$ cluster means a positive charge, according to the Kröger-Vink notation [29] and this charge occurs because the Mo cations has formal charge of 6+, Mo (VI), while in the Ag_3PO_4 structure, the P cation has a formal charge 5+, P(V). This positive charge induces the formation of dipoles between the $[MoO_4]\cdot$ and $[PO_4]$ clusters, which in turn cause a high electronic repulsion. We were able to build theoretical models of the samples using the results from Rietveld analysis (Fig. 2). As can be seen in Fig. 2, the Ag_3PO_4:Mo model presents symmetric tetrahedral $[PO_4]$ clusters whereas the $[MoO_4]\cdot$ clusters are distorted. This symmetry breaking process and the distortion of the lattice at medium range is a

Table 1
Rietveld refinements of Ag_3PO_4 and Mo-doped powders.

Sample	Lattice Parameters		Cell volume $(Å)^3$	R_{Bragg}	χ^2	R_{wp}	R_p
	a = b = c (Å)	(%)					
Ag_3PO_4	6.01514(2)		217.640(2)	0.049	1.992	0.091	0.065
Mo 0.5%	6.01582(2)		217.713(2)	0.039	1.872	0.079	0.058
Mo 1%	6.01614(3)		217.748(3)	0.022	1.868	0.104	0.073
Mo 2%	6.01798(4)		217.948(5)	0.045	1.833	0.083	0.058
Ag_3PO_4		6.004(2)	216.4(2)	–	–	–	–

consequence of the interaction between the $[MoO_4]\cdot$ and $[PO_4]$ clusters.

The formation energy, ΔE_f, can be related to the existence of stable crystal. Furthermore, the negative values of ΔE_f indicates the presence of stronger bonding between the atoms and more alloying stability of the crystal [30]. The values of ΔE_f for pure Ag_3PO_4 and Ag_3PO_4:Mo 6.5% are -26.912 and -26.382 Ry/a.u^3 (see Table SI-1). The negative value of E_f represents the ground state structural stability of a system. The undoped (pure) system shows more stability as compared to doped one with higher values of negative ΔE_f. This result was expected, once that the Mo atoms caused a local disorder, as discussed above.

3.2. Raman spectroscopy

Raman spectroscopy is considered a powerful technique for estimating the local structural order (*i.e.*, short-range order) of solids. Fig. 3 displays the experimental spectra obtained from CP synthesized pure Ag_3PO_4 and Ag_3PO_4:Mo 0.5, 1, and 2% samples. The results compare very well to the spectra reported by Botelho et al. for Ag_3PO_4 powders synthesized using CP and subsequently processed in a microwave-assisted hydrothermal (MAH) system [11]. The authors performed a full theoretical calculation of the Raman shifts, enabling an unambiguous assignment of the observed lines. Eighteen Raman-active modes were predicted for the Ag_3PO_4 structure, however, only six of these modes were observed because of overlapping lines and/or because of their low

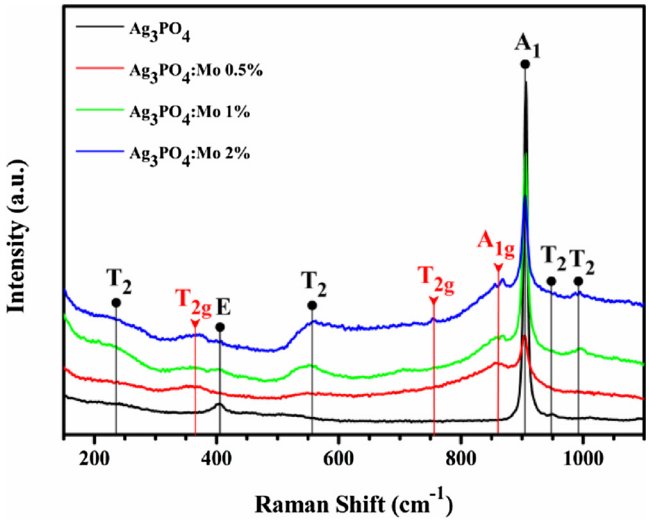

Fig. 3. Raman spectra of Ag_3PO_4, Ag_3PO_4:Mo 0.5%, Ag_3PO_4:Mo 1%, and Ag_3PO_4:Mo 2%.

intensities. Therefore, the 905 cm^{-1} line was assigned to the symmetric stretching vibration mode of the $[PO_4]$ cluster (A_1), while those at 948 (very weak) and 991 cm^{-1} were assigned to the T_2 asymmetric

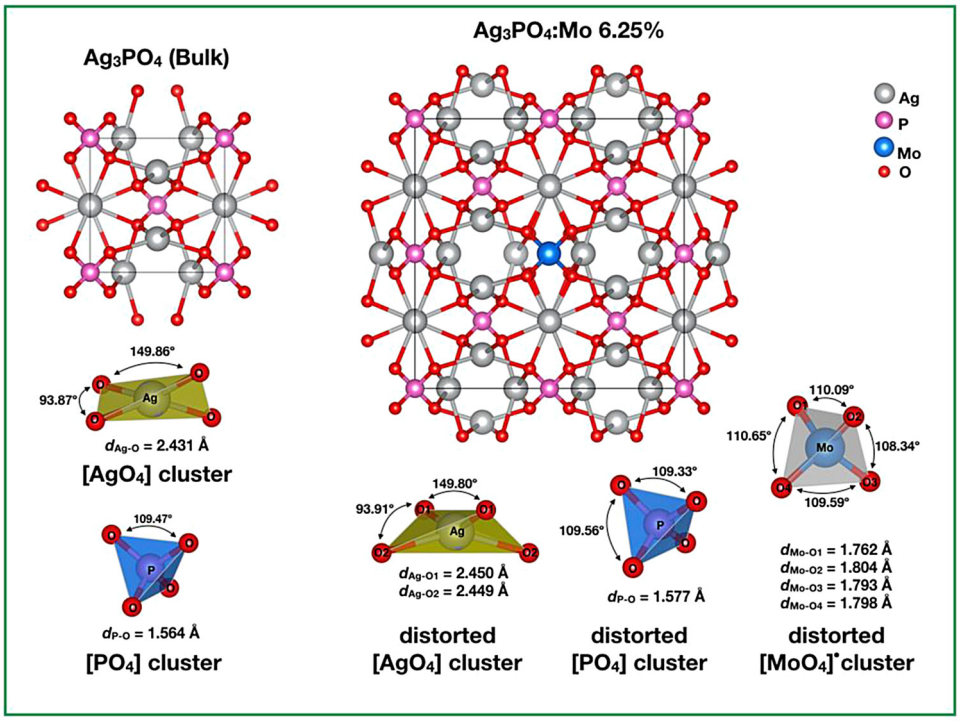

Fig. 2. Schematic representation of Ag_3PO_4 (bulk) and Ag_3PO_4:Mo supercell models.

stretching modes (ν_3 and ν_1 modes of the free tetrahedron, respectively). The 404 and 557 cm^{-1} lines were the symmetric (E) and asymmetric (T_2) bending modes of the [PO_4] cluster (ν_2 and ν_4 modes of the free tetrahedron, respectively), and the 237 cm^{-1}line (T_2) was a vibration mode (rotation and/or translation of the [PO_4] tetrahedron). An additional, very weak line observed at 709 cm^{-1} in [11] was attributed to the symmetric stretching vibration of the O—P—O bonds or, alternatively, to a combination mode. These assignments were in agreement in most cases with previously reported data [31,32].

In the Ag_3PO_4:Mo samples, additional lines appear around 860, 756 (very weak), and 364 cm^{-1}. Those correspond to the typical lines of β-Ag_2MoO_4 (A_{1g}, T_{2g}, and T_{2g}, respectively), as reported in the 300–900 cm^{-1} range [33–35]. Their intensities increase with Mo doping concentration, in agreement with the increase in [MoO_4] tetrahedral cluster content. Meanwhile, the most interesting feature was the strong increase in the intensity of the broad line near of 550 cm^{-1} (asymmetric bending of [PO_4]). According to Mroczkowska et al. a departure from the original T_d symmetry of the [PO_4] tetrahedra leads to the increase in intensity of certain Raman lines, especially the asymmetric ones [31]. Indeed, they observed a clear increase in the lines near 550 and 980 cm^{-1} when doping Ag_3PO_4 with AgI. We observed the same phenomenon in our Mo doped samples (especially around 550 cm^{-1} where $[MoO_4]^{2-}$ does not present any lines), suggesting that Mo(VI) actually entered into the Ag_3PO_4 structure. Moreover, it should be noted that the weak line near 364 cm^{-1} (asymmetric bending of $[MoO_4]^{2-}$ [33]) was considerably exalted, even in the low-doped Ag_3PO_4:Mo 0.5% sample, suggesting a local loss of symmetry compared to pure Ag_2MoO_4.

3.3. XPS analysis

We performed XPS analysis of the pure Ag_3PO_4 and Ag_3PO_4:Mo 0.5, 1, and 2% samples in order to evaluate their chemical composition and surface valence states. Fig. 4(a) shows the survey spectra of all samples. The presence of the main binding-energy peaks of Ag, P, and O was observed in the pure sample and the Mo peaks were observed in the Mo-doped samples. In all the cases, C related peaks were also observed. These were ascribed to the carbon pollution from the XPS instrument. No peaks related to other elements were identified, confirming that the prepared samples were only composed of Ag, P, O, and Mo.

Figs. 4(b–d) show the high-resolution XPS spectra of Mo in the Ag_3PO_4:Mo 0.5, 1, and 2% samples. In these spectra, the peaks at ~236.0 and ~232.8 eV were similar to those of pure α-MoO_3, which were ascribed to the characteristic binding energies of Mo $3d_{3/2}$ and Mo $3d_{5/2}$ doublet, respectively, caused by the spin-orbit coupling. Hence, the binding energy separation of the Mo 3d peaks was ~3.2 eV, which is best related to the oxidation state of Mo(VI). The presence of these peaks might stem from the accommodation of Mo(VI) into the Ag_3PO_4 lattice. Moreover, a shift in both peaks was observed compared to the Mo 3d spectrum measured in a pure β-Ag_2MoO_4 sample (see Supporting Information, Fig. SI-3) with the data in the literature [36], as well as the data for Ag_3PO_4/β-Ag_2MoO_4 composites reported by Cao et al. [10]. These results could be associated with the strong interaction between the Mo(VI) dopant and the Ag_3PO_4 structure. Namely, the Mo(VI) cation substituted the P(V) cation in [PO_4] tetrahedral clusters, and the electronic density of Mo(VI) was disturbed when compared to the one present in the [MoO_4] tetrahedral clusters in the β-Ag_2MoO_4 structure.

We employed XPS as an appropriate tool to demonstrate the presence of Ag with distinct valence states on the surface of the Ag_3PO_4 samples. Fig. 4(e) shows the high-resolution XPS spectra in the 3*d* region of Ag for the pure and Mo-doped samples. The peaks at ~374 and ~368 eV were associated with the binding energies of the Ag $3d_{3/2}$ and Ag $3d_{5/2}$ doublets, respectively. Moreover, each of these peaks could be fitted into two separate components, indicating the presence of Ag with different oxidation states. The components at 374.8 and 368.8 eV are related to Ag°, and the ones at 373.9 and 367.8 eV can be assigned to Ag^{+} [37–39]. The percentages of Ag° on the surface of the Ag_3PO_4 particles were 11.5, 13.7, 12.8, and 12.2% for the Ag_3PO_4 and Ag_3PO_4:Mo 0.5, 1, and 2% samples, respectively. We observed a clearly increasing tendency for the formation of metallic Ag for the Mo-doped samples, where the highest concentration of this species corresponded to the Ag_3PO_4:Mo 0.5% sample (13.7%). The concentration of Ag° on the surface of the particles could most likely be associated with the disorder induced by the Mo(VI) dopant in the Ag_3PO_4 structure, which facilitated the reduction of Ag^{+} to Ag°. This event takes places because of the interaction of samples with the electromagnetic wave used in XPS characterization.

Fig. SI-4 (a–d) shows the high-resolution XPS spectra for O in the

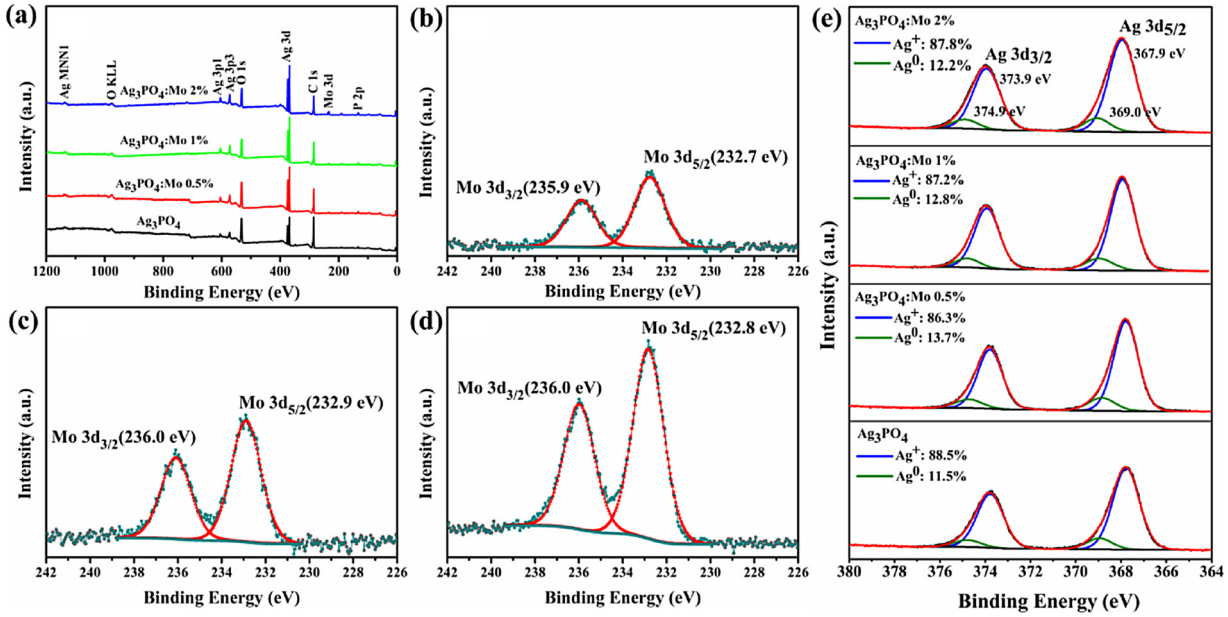

Fig. 4. XPS survey spectra of pure (black line) and Mo^{6+} doped (increasing amount from the bottom to top) Ag_3PO_4 microcrystals **(a)** and XPS spectrum of Mo 3d for Ag_3PO_4:Mo 0.5% **(b)**, Ag_3PO_4:Mo 1% **(c)**, Ag_3PO_4:Mo 2% **(d)** samples and **(e)** XPS spectra of Ag 3d for Ag_3PO_4, Ag_3PO_4:Mo 0.5%, Ag_3PO_4:Mo 1% and Ag_3PO_4:Mo 2% samples.

pure and Mo-doped samples. As shown in Fig. SI-4 (a), for the pure Ag_3PO_4 sample, the O 1 s peak was best fitted into three separate components with binding energies of 533.0, 531.7, and 530.4 eV, which could be respectively assigned to the adsorbed water molecules, surface hydroxyl groups, and lattice oxygen of the O—P bonds in the Ag_3PO_4 structure [40–43]. These components were also observed in all doped samples (see Supporting Information, Fig. SI-4(b–d)), and could be attributed to the same chemical constituents in pure Ag_3PO_4. However, when increasing the Mo(VI) concentration we also noticed a tendency toward a positive shift in the binding energy of the O 1s component corresponding to the lattice oxygen. This shift reached a total value of 0.4 eV in the highest doped sample (530.8 eV in Ag_3PO_4:Mo 2% sample). Moreover, this behavior was associated with a crescent increment in intensity of this oxygen peak compared to the other O 1 s components. According to the literature [36,44,45], these results could be attributed to the presence of lattice oxygen corresponding to the O–Mo bonds, reinforcing the assertion of an actual doping of the Ag_3PO_4 structure. The high-resolution XPS spectra for P in Fig. SI-5 (a–d) (Supporting Information) shows the P 2p peak at ~132.9 eV corresponding to the binding energy of P(V) in Ag_3PO_4 [42].

The atomic composition was further quantified by fitting the integrated peak areas and applying calibrated atomic sensitivity factors for each element. The results of these quantifications are listed in Table 2. The Mo concentrations obtained for the Mo-doped samples were very close to the atomic concentration of Mo dopant added in the solution. Interestingly, it can also be noted that the Ag/P atomic ratio gradually increased with the increase in Mo concentration, suggesting the substitutional doping of Mo(VI) for P(V). Moreover, Ag/P atomic ratio are lower than 3 for all cases. No secondary phases were evidenced by XRD and Raman characterization, even in the form of small crystallites as observed in TEM analysis (see sections below). It is important to emphasize that XPS is a surface technique. A plausible explanation is the presence of distinct compositions of pure and Mo-doped Ag_3PO_4 particles comparing their bulk and surface regions, which is typically observed in Ag-based complex oxides [46,47]. This phenomenon arises due to the terminations from distinct crystallographic planes that are exposed at the surface, which can be richer in $[PO_4]$ than bulk, lowering the overall Ag/P ratio at the surface. Moreover, adsorbed species such as water can interfere in the quantitative results, resulting in the depart from the ideal values predictable for Ag_3PO_4 stoichiometry.

3.4. FEG-SEM, BET and TEM analyses

Fig. 5 displays the FEG-SEM images of our Ag_3PO_4, and 0.5, 1 and 2% Mo-doped samples. The particles are mainly round with an average diameter in the 300–450 nm range (Table 3 and Fig. SI-6), with a trend for Ag_3PO_4:Mo 0.5% to present slightly smaller, relatively monodisperse particles. Moreover, some quite well-formed cubic crystals (pure Ag_3PO_4) can be seen in all samples, as well as edge-truncated cubes (Ag_3PO_4:Mo 0.5%) and more complex geometries for the 1 and 2% doped samples. It should be noted that the shape evolution of these crystals followed the morphologies calculated by Botelho et al. [12] when the surface energy of the (100) plane increased. Substituting PO_4^{3-} with MoO_4^{2-} obviously resulted in localized defects, which, in turn, could modify the energy of the various crystal planes, thus influencing the morphology of the particles.

Table 2
Elemental identification and quantification estimated by XPS of the various samples.

Sample	Ag (at%)	P (at%)	Mo (at%)	O (at%)	Ag/P
Ag_3PO_4	12.9	9.2	–	77.9	1.4
Mo 0.5%	16.1	10.4	0.6	72.9	1.5
Mo 1 %	20.7	10.9	1.1	67.3	1.8
Mo 2%	22.9	11.7	3.2	62.2	2.0

In this study, we also calculated S_{BET} and estimated the particle size of Ag_3PO_4 and Ag_3PO_4:Mo 0.5% samples. The 77 K N_2 adsorption-desorption isotherms are shown in Fig. SI-7, and the main results are listed in Table 3. As expected, the Ag_3PO_4:Mo 0.5% particles shows higher adsorption than Ag_3PO_4 particles, given the highest S_{BET} for 0.5% doped sample. This behavior also reflects in the particle sizes of the samples, where a decrease from 570 to 500 nm is observed by doping with 0.5%. This result corroborates with the estimation obtained by FEG-SEM. It was also observed that the particle sizes calculated by BET analysis are slightly larger than those obtained by FEG-SEM. The principal reason for this discrepancy is the tendency of some particles to agglomerate, which will increase the particle size estimation by BET analysis.

We performed TEM analysis using Ag_3PO_4:Mo 2%, the sample with the highest Mo content in the crystalline lattice of Ag_3PO_4 that was synthesized without a secondary phase. Fig. 6(a) shows a TEM image of this sample, and Fig. 6(b) a high-magnification TEM image in a border region of a single particle. The inset in Fig. 6(b) shows the high-resolution TEM (HR-TEM) image of this site, where the 0.25 nm interplanar distance corresponds to the (211) plane of Ag_3PO_4. Fig. 6(c) and (d) displays the HAADF-STEM and EDS maps of several particles obtained from the Ag_3PO_4:Mo 2% sample. It can be seen that these samples are very homogeneous, and their Mo content shows no sign of segregation. On the bottom of the micrograph there are two curled outgrowths that are clearly composed of metallic silver. These are due to the electron beam reduction of Ag_3PO_4 as studied in detail by Botelho et al. [11] and previously reported in several silver-containing oxide ceramics [48–51].

In order to further analyze these crystalline outgrowths, HR-TEM was performed, as shown in Fig. 7. The nanostructures have very well-defined edges and planes, which indicate a single-crystalline nature. The interplanar 0.23 nm distance (inset of Fig. 7), is indexed with the {111} planes family of cubic structure Ag, belonging to the $Fm\ \bar{3}\ m$ space group according to the ICSD database No. 604630 [52]. The fast Fourier transformed (FFT) image from the same location also shows the {331}, {311}, and {400}, plane families associated with 0.09, 0.12, and 0.10 nm distances, respectively. These data confirmed the presence of small metallic Ag crystals growing on the surface of the Ag_3PO_4 mesostructure, however the amount was too small to be detectable in XRD patterns.

3.5. UV–vis diffuse reflectance spectroscopy

The UV–vis absorption spectra of the pure Ag_3PO_4 and Mo doped samples are reported in Fig. SI-8 (Supporting Information). The band gap (E_{gap}) values of the Ag_3PO_4 and Ag_3PO_4:Mo samples were experimentally estimated by extrapolating the linear portion of the UV–vis curves using the Kubelka − Munk function [53]. Theoretical and experimental studies have reported that Ag_3PO_4 powders exhibit indirect allowed electronic transition, with E_{gap} = 2.36 eV [6]. Therefore, in the well-known relationship $\alpha h\nu = C_1(h\nu\text{-}E_g)^n$, the condition n = 2 was adopted. Table 4 presents the experimental and theoretical band gap values for the Ag_3PO_4 and Ag_3PO_4:Mo samples.

Fig. SI-8 shows that for our pure Ag_3PO_4 sample, the gap is 2.16 eV, the same value as previously reported by Botelho et al. [11] for CP prepared Ag_3PO_4. This lowering of E_{gap} is the signature of the formation of intermediate states in the forbidden band, due to defects. Indeed, as reported by Botelho et al. [11], E_{gap} increased up to 2.25 eV when the defects in the pristine sample were cured by the use of a MAH process. It is worth noting that the doping of Ag_3PO_4 with Mo(VI) provoked a significant decrease in E_{gap}, especially for the Ag_3PO_4:Mo 0.5% sample with E_{gap} = 2.07 eV.

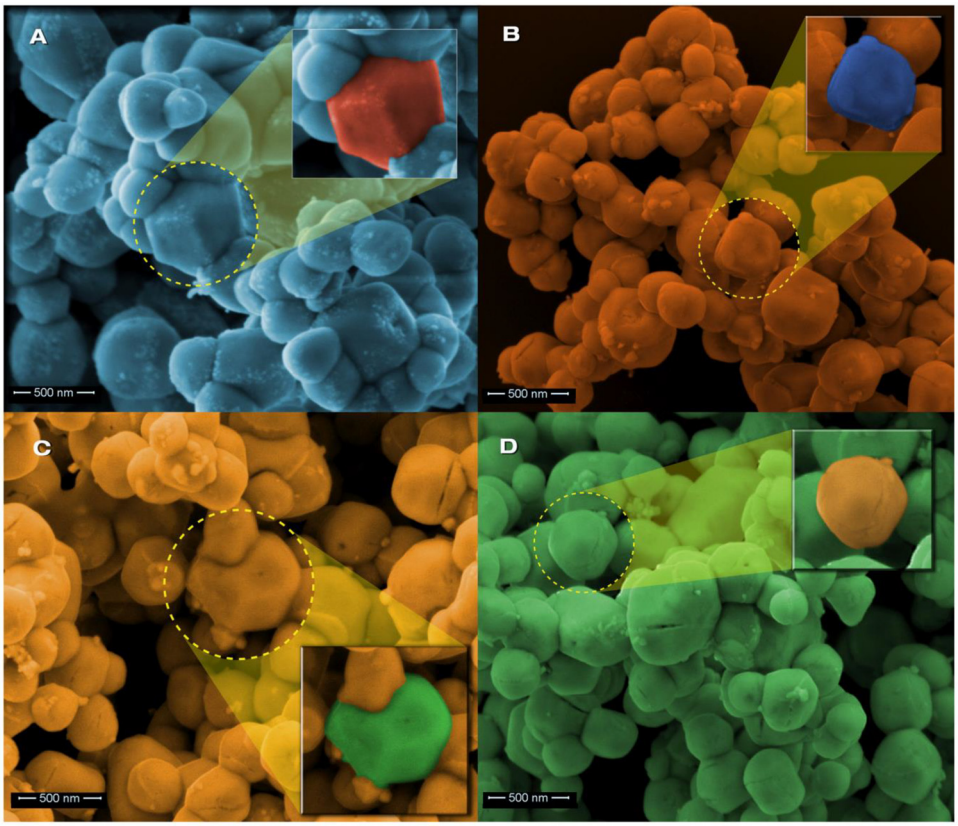

Fig. 5. FEG-SEM images of **(a)** Ag_3PO_4, **(b)** Ag_3PO_4/Mo 0.5%, **(c)** Ag_3PO_4/Mo 1% and **(d)** Ag_3PO_4/Mo 2%.

Table 3
. Surface area and particle size values obtained by BET and particle size values obtained by FEG-SEM for the samples of Ag3PO4 and Ag3PO3: Mo 0.5%.

	BET		FEG-SEM
Sample	Surface Area (m^2/g)	Particle Size (nm)	Particle Size (nm)
Ag_3PO_4	1.64	570	453
Ag_3PO_4:Mo 0.5%	1.87	500	333

3.6. Band structure and DOS

The analyses of the electronic levels that comprise the band structure were evaluated by theoretical calculations. The bulk optimized Ag_3PO_4 presented an indirect 2.54 eV band gap, as found experimentally and described theoretically in the literature [11,54,55], between the M–Γ points. It is important to emphasize that this value was slightly higher compared to the other reported values [55,56]. Using the optimized structural parameters, a supercell with a 2 × 2 × 2 matrix was built and the structure was re-optimized. Subsequently, the Ag_3PO_4:Mo model was built as described above in computational methods. Fig. 8 illustrates the band structure of the pure Ag_3PO_4 and Ag_3PO_4:Mo supercells.

It is well-known that the presence of impurities or local defects can decrease the band gap due to the creation of new intermediate levels between the VB and CB [35,57]. To simulate the Ag_3PO_4 structure with Mo doped into the lattice, it was necessary to expand the matrix up to sixteen instead of two Ag_3PO_4 units in the bulk as mentioned above. During the optimization process, the field force generated by the expansion stabilized the direct band gap between the Γ points. However, the band gap value remained at 2.54 eV for Ag_3PO_4. In the Ag_3PO_4:Mo model, a decrease of the band gap value to 2.44 eV was observed, as expected. A similar decrease was experimentally observed for the Ag_3PO_4:Mo samples synthetized using the CP method that is associated with the formation of new levels in the forbidden gap.

Using DOS analysis it is possible to determine the orbital composition of the different electronic levels in the VB and CB that composed the band structure. Fig. 9 illustrates the total DOS for the pure Ag_3PO_4 and Ag_3PO_4:Mo supercells. For the pure Ag_3PO_4 supercell, the top of the VB was constituted mainly by the Ag 4*d* orbitals and the O $2p_y$ and $2p_z$ orbitals, while the bottom of the CB is formed by the *s* orbitals of all atoms (Ag, P and O). In the Ag_3PO_4:Mo model, the top of the VB is constituted only by the Ag $4d_z^2$, $4dx^2$-y^2, and 4*dxy* orbitals and only the O $2p_y$ orbitals. The bottom of the CB is continuous with the *s* orbital contributions from the Ag, P and Mo atoms, except for the O 3*s* orbitals, and a contribution from $4d_z^2$ orbitals from Mo atoms. Therefore, the main change in the DOS due to the presence of Mo(VI) in the Ag_3PO_4 structure was the break in degeneracy in the Ag 4*d* orbitals and the presence of the 4*d* orbitals from the Mo(VI) atoms in the CB provokes the decrease of the band gap value.

3.7. PL emissions

Fig. 10 shows the PL spectra of various samples obtained at room temperature under UV excitation. The spectra consist of a broad band that can be deconvoluted into two main contributions centered around 450 nm (blue component) and 520 nm (green component), suggesting a multilevel process involving the participation of several energy levels within the band gap [12]. The blue component was attributed to the [PO_4] clusters (lattice former) [11,12]. Indeed, a similar band was observed for Ag_2MoO_4 and was related to the charge transfer transition within the regular [MoO_4] tetrahedron [53]. The green component should be related to intermediate energy levels [11]. Moreover, a very weak red component near 630 nm that was associated with the highly distorted [AgO_4] clusters [12] can be seen. A very strong PL emission near 650 nm was previously reported for Ag_2MoO_4/Ag_2WO_4 core-shell

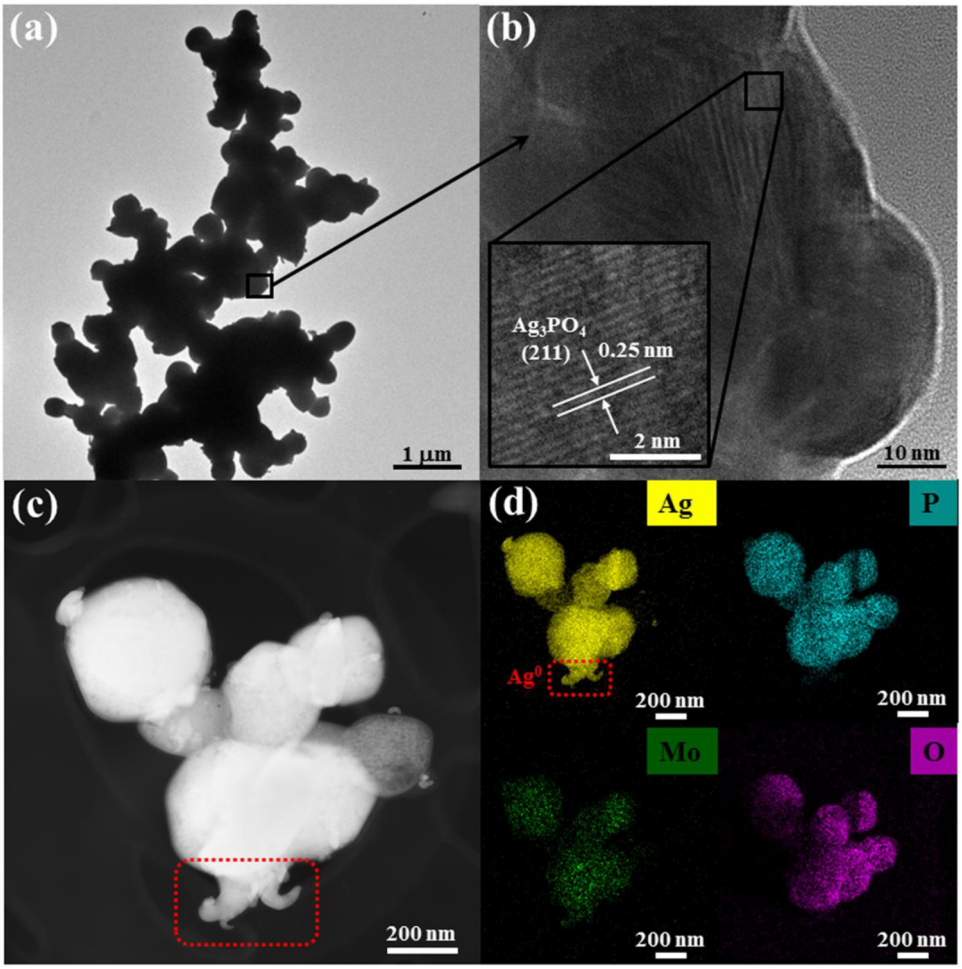

Fig. 6. TEM images of **(a)** Ag_3PO_4:Mo 2%, **(b)** characteristic interplanar distance of Ag_3PO_4, **(c)** and **(d)** EDS maps of a group of particles in Ag_3PO_4:Mo 2%.

nanocomposites, and was attributed to the structural defects (distortions) at the interface between the two compounds [58]. Thus, this red emission could be in part a signature of the growth of very small Ag_2MoO_4 crystals on the surface of the doped samples. Such a mechanism could not be ruled out, although the presence of Ag_2MoO_4 could not be detected at this level by XRD and was not evidenced in the SEM images. In addition, this component may be related to the deep defects that were generated in the sample. Vacancies, interstitial atoms, displacements, grain contours or precipitates generate these deep defects, in which the electrons can be trapped, allowing the release of

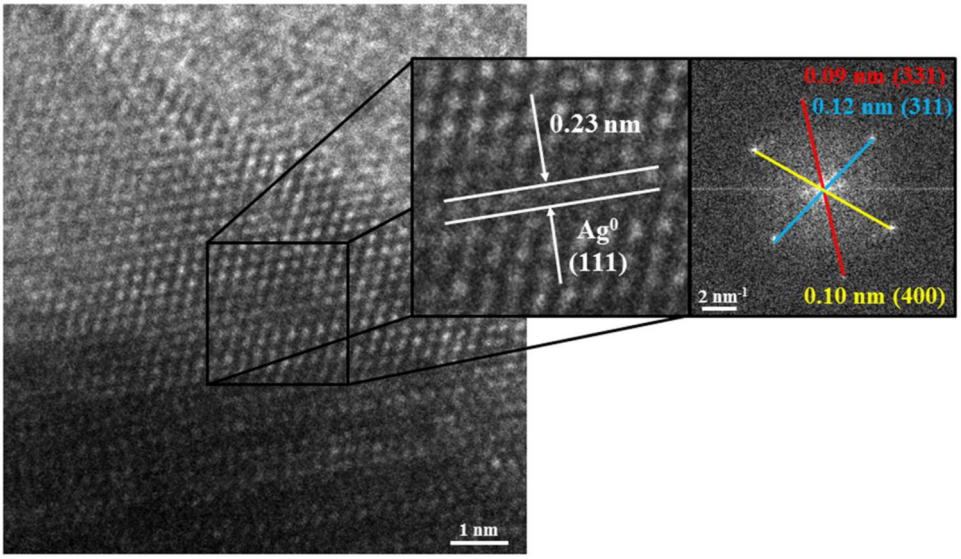

Fig. 7. HR-TEM images of the outgrowth visible on Fig. 6(c) and (d), showing a characteristic interplanar distance and the associated electron diffraction pattern.

Table 4
Experimental and theoretically calculated (into brackets) band gap values for pure Ag_3PO_4 and Mo-doped Ag_3PO_4 samples.

Sample	E_{gap}
Ag_3PO_4	2.16 (2.54)
Ag_3PO_4 :Mo 0.5%	2.07
Ag_3PO_4 :Mo 1%	2.11
Ag_3PO_4 :Mo 2%	2.12
Ag_3PO_4 :Mo 6.5%	(2.44)

energy in the form of a photon.

The insets in Fig. 10 illustrate the intensity ratios of the three components: the red contribution increases from 1.7 to 18.4% for the 0 and 0.5% doped samples, then slightly decreases to 7.4 and 10.2% for the 1 and 2% doped samples. This evolution, with a special value for the 0.5% Mo doped sample, is clearly comparable to the values of E_{gap}.

3.8. Photocatalytic activity of Ag_3PO_4:Mo microcrystals

The photocatalytic activity of Ag_3PO_4 as well as those of materials doped with different amounts of Mo were tested for the degradation of RhB under visible light irradiation. For comparison, when RhB was subjected to visible light irradiation, under the same experimental conditions, without the presence of a catalyst, its degradation of RhB was practically insignificant.

Samples were collected after different times (0, 5, 10, and 15 min) of visible light irradiation and were analyzed by UV–vis spectroscopy. The results are shown in Fig. 11. The time-dependent absorbance of RhB in the presence of Ag_3PO_4 and Ag_3PO_4:Mo shows the RhB characteristic peak located at 553 nm decreasing with time.

Fig. 12(a) shows the variations in the concentration of RhB (C_N/C_0) *versus* irradiation time when in contact with various catalysts; C_0 and C_N are the equilibrium adsorption concentration and the concentration after the irradiation time (t), respectively. It can be seen that RhB underwent faster degradation in the presence of Ag_3PO_4:Mo 0.5%: approximately 92% degradation after only 5 min of irradiation. By contrast, Ag_3PO_4 without dopant degraded only 55% during the same time, showing that doping provided a significant improvement in the photodegradation of RhB.

To quantitatively compare the samples, kinetic analysis was performed using the Langmuir-Hinshelwood model, defining a pseudo first order reaction because the initial concentration of the dye was relatively low [59]:

$$-\ln(C_N/C_0) = k't \quad (2)$$

where k' and t represent the constant reaction rate (pseudo first order) and the irradiation time, respectively (Fig. 12(b)). Table 5 summarizes the results. The reaction constant for Ag_3PO_4:Mo 0.5%, which was clearly the compound with the optimal Mo-doping amount, was 0.347 min^{-1}. This catalyst had the highest rate constant, almost two times higher than that of the pure Ag_3PO_4 sample.

The degradation of dyes using photoactive materials in an aqueous solution mainly depends on the band gap, surface area, amount of the catalyst, and generation of an electron – hole ($e^-h\cdot$) pair. The activation of the semiconductor photocatalyst is achieved through the absorption of a photon of ultra-band gap energy, which results in the promotion of an electron *e-* from the VB to the CB, with the concomitant generation of a hole ($h\cdot$) in the VB. For a semiconductor photocatalyst to be efficient, the different interfacial electron processes involving *e-* and $h\cdot$ must compete effectively with the major deactivation processes involving *e–*$h\cdot$ recombination. In the case of Ag_3PO_4, it is well known that this catalyst presents a negative surface, which means that it is well suited to attract $h\cdot$ and repel the electrons [60]. In addition, the electrons have lower effective mass – therefore, they display a greater mobility with respect to $h\cdot$ [61,62].

It has been observed that the surface area plays a major role by providing a higher adsorption of dye molecule on the surface of photocatalyst and enhances the photocatalytic activity. The higher catalytic activity of Ag_3PO_4:Mo 0.5% may be partly related to the particle diameter. As shown in Table 3, this sample presents a much smaller diameter, which results in a larger surface area. Such conclusion was supported by, the BET analysis. Therefore, it is possible to expect that this sample possesses more active sites for the degradation of RhB. However, the afore mentioned results showed that this catalyst had a lower E_{gap} value, an argument for better photocatalytic activity under visible light irradiation.

Several studies have highlighted that oxidant species such $h\cdot$ and superoxide ions (O_2') play key roles in the photocatalytic action when Ag_3PO_4 is used as a photocatalyst [63–66]. In order to propose a photocatalytic mechanism, tests of photocatalytic activity were performed with the addition of appropriate reactive species scavengers. Then, we used BQ to capture O_2', AO as $h\cdot$ eliminator and TBA to capture hydroxyl radicals (OH^*), respectively. The Ag_3PO_4:Mo 0.5% sample was chosen for this study, as it presented the best photocatalytic response. The pure Ag_3PO_4 sample was also selected in order to analyze the influence of the dopant on the photodegradation mechanism. The results are shown in Fig. 13(a). As seen in this figure, with the addition of TBA in the Ag_3PO_4:Mo 0.5% reaction mixture, the degradation reached 100% after 15 min, suggesting that OH^* was not the main reactive

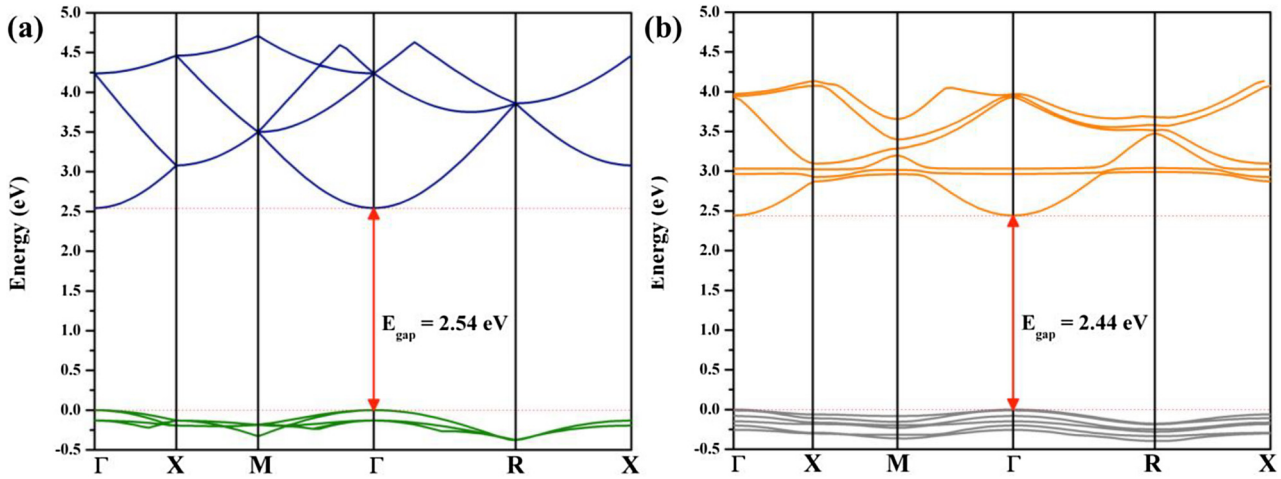

Fig. 8. The band structure of pure Ag_3PO_4 and Ag_3PO_4:Mo supercells.

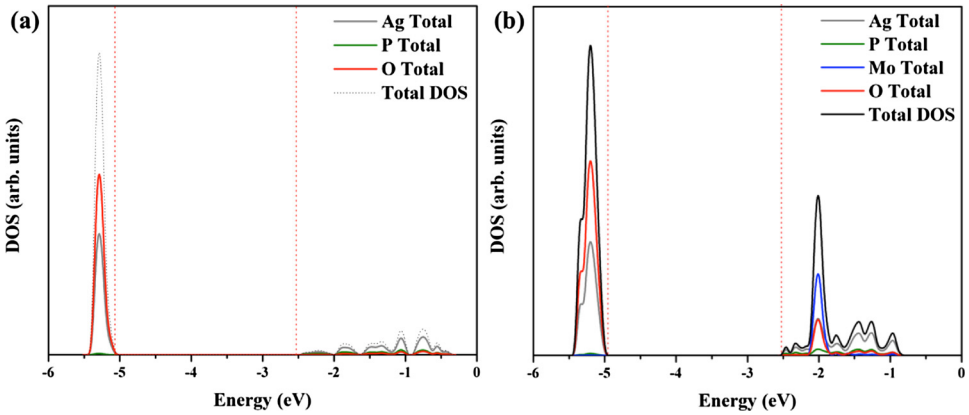

Fig. 9. The total DOS for the pure Ag_3PO_4 and Ag_3PO_4:Mo supercells.

species in the process. In addition, IPA was used as another OH^* scavenger and the result was the same as when TBA was used. However, when we added TBA to the reaction mixture of Ag_3PO_4, we obtained a significant decrease in the degradation rate. The same occurred when we added IPA, but the decrease in degradation was not as remarkable as it when using TBA. This can be explained by the chain size of each compound. TBA has a tertiary carbon and IPA a secondary carbon. As a consequence, TBA captures more OH^* species, reducing dye degradation. These results suggest that OH^* species play a role in the photodegradation process.

When BQ and AO were added to the reaction system, as O_2' and $h\cdot$ scavengers, respectively, the degradation rate decreased more significantly than for the OH^* scavengers. This suggested that the direct transfer of phosphate holes and the transfer of simple electrons to generate O_2' radicals were the dominant mechanisms responsible for this photocatalytic activity in both materials. This behavior was also reported by Zhang et al. [67] for Ag_3PO_4/NG/P3HT doping. These results clearly contrasted with those reported by Cao et al. [10] for β-Ag_2MoO_4/Ag_3PO_4 composites, where only $h\cdot$ played a critical role in the degradation process of RhB when more than 5% (in weight) composite material was used.

Pure Ag_3PO_4 is not intended for industrial use because it does not exhibit good photocatalytic stability [6]. In order to evaluate the photocatalytic stability of the proposed material, photocatalysis cycles were performed, reusing the material. Tests were run using Ag_3PO_4 and Ag_3PO_4:Mo 0.5% samples. During the first test, recovering the powder from the first cycle and following the same experimental procedure described above, we observed that even in the absence of visible light irradiation, significant degradation of the dye occurred for both catalysts (see Supporting Information, Fig. SI-9(a)). We performed XRD after each cycle (see Supporting Information, Fig. SI-9(b)) and observed peaks suggesting the presence of metallic Ag and/or Ag_2O that were not previously detected. This behavior has already been reported by Botelho et al. [12]. They reported that the sample, initially yellow, became grey after the cycle, due to the formation of metallic Ag on its surface. Both metallic Ag and Ag_2O particles on the surface appeared due to light exposure during the previous cycle that led to structural modifications and surface defects, which could, in turn, act as active

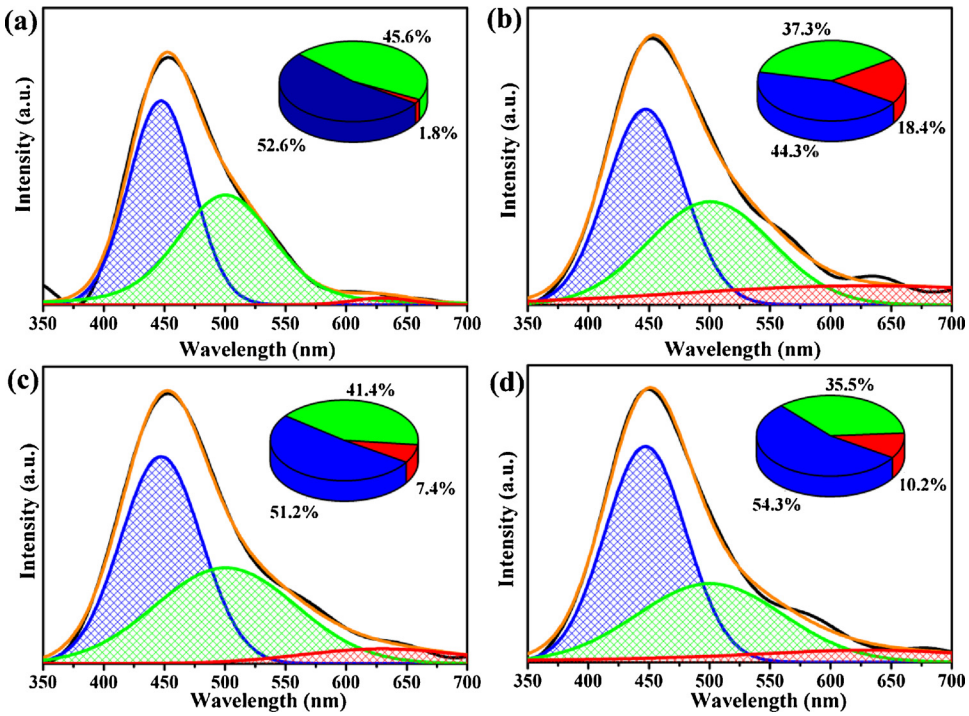

Fig. 10. Photoluminescence spectra (black line = experimental data) for **(a)** Ag_3PO_4, **(b)** Ag_3PO_4:Mo 0.5%, **(c)** Ag_3PO_4:Mo 1% and **(d)** Ag_3PO_4:Mo 2%. Their deconvolution gives three peaks (orange line = sum), the distribution of them is given in inset.

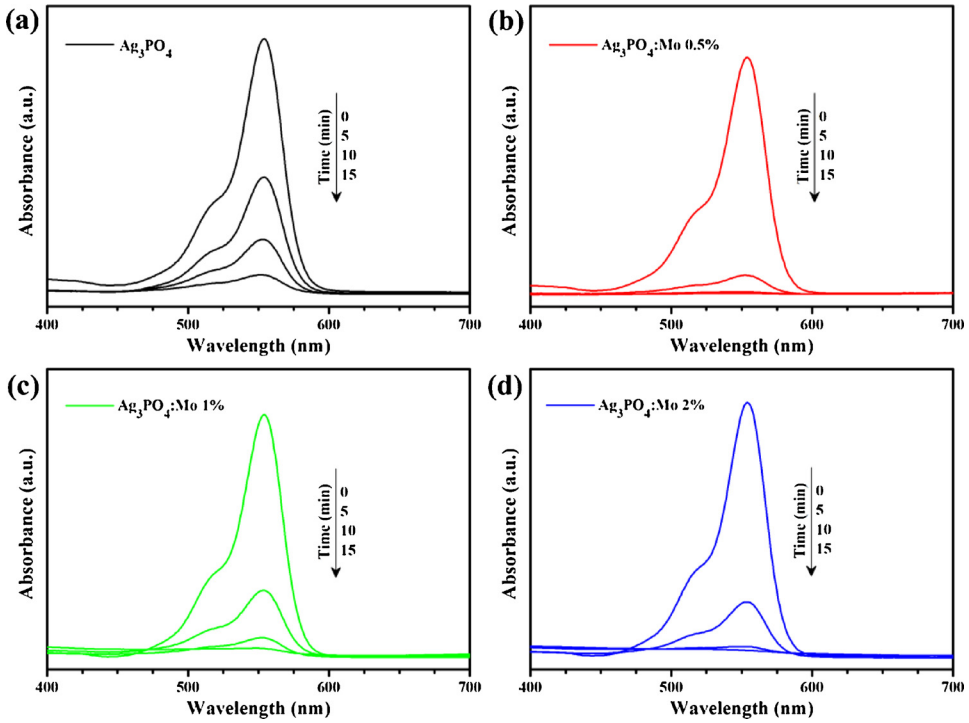

Fig. 11. UV–vis absorption spectra of RhB upon photodegradation in the presence of **(a)** Ag_3PO_4, **(b)** Ag_3PO_4:Mo 0.5%, **(c)** Ag_3PO_4:Mo 1% and **(d)** Ag_3PO_4:Mo 2% catalysts.

sites to degrade the dye.

To minimize this effect of dye degradation in the dark, the experimental procedure for the second and third photocatalysis cycles was modified. The 30 min corresponding to the dark adsorption equilibrium time was suppressed, as the partial discoloration of RhB by the Ag/Ag_2O formed in the previous cycle could be produced even without the presence of light. Fig. 13(b) shows the results of this new procedure. The unexpected shift at time $t = 0$ is now suppressed (see Supporting Information, Fig. SI-9 (a)). It can be noticed that from the second cycle, Ag_3PO_4 without dopant tends to improve its catalytic response due to the growth of elemental Ag as mentioned above. To minimize this effect of dye degradation in the dark, the experimental procedure for the second and third photocatalysis cycles was modified. The 30 min corresponding to the dark adsorption equilibrium time was suppressed, as the partial discoloration of RhB by the Ag/Ag_2O formed in the previous cycle could be produced even without the presence of light. Fig. 13(b) shows the results of this new procedure. The unexpected shift at time t = 0 is now suppressed (see Supporting Information, Fig. SI-9(a)). It can be noticed that from the second cycle, Ag_3PO_4 without dopant tends to improve its catalytic response due to the growth of elemental Ag as mentioned above. Appearance of elemental Ag is also observed for doped sample, as seen in Fig. SI-9(b), and we note that the peak is more intense than the pure material; there is a larger formation of metallic Ag in the doped material than in the pure material. This observation helps us understand why doped material exhibits a small loss of photocatalytic activity compared to the pure material. Ag° is formed mainly at the active sites on the surface of the material, protecting the absorption of light and thus reducing the rate of degradation of the dye. At some point, Ag° can be considered an agent that favors photocatalysis, which is observed in the pure material. However a very large amount of Ag° formed can decrease the photocatalytic efficiency of the material, as seen on the doped sample. Moreover, it can be noticed that Ag_3PO_4:Mo 0.5% is stable during the cycles, while Ag_3PO_4 loses some of its catalytic efficiency in the third cycle.

The mineralization degree of prepared samples towards organic contaminants was further investigated. Fig. 13(c) shows the total organic carbon (TOC) removal results on the photocatalytic degradation of RhB with Ag_3PO_4 e Ag_3PO_4:Mo 0.5% catalysts. The removal of TOC reached up to 52.41 and 32.34% within 30 min of visible light irradiation for Ag_3PO_4:Mo 0.5% and pure Ag_3PO_4 catalysts. These results clearly demonstrated the improved mineralization activity for 0.5% doped sample in compare to the pure one. It is important to emphasize that the catalysts first degrades the chromophores present in the dye. Hence, the mineralization activity was slower in comparison with degradation rate, and for a total TOC removal more time of illumination is needed.

3.9. Possible photocatalytic mechanism for the degradation of RhB

As observed in the previous sections, our Ag_3PO_4:Mo crystals obtained by CP method have distinct types of defects, which induced changes in the symmetry of the $[AgO_4]$, $[PO_4]$, and $[MoO_4]$ clusters in bulk and on the surfaces. This behavior allowed the polarization of the material with the formation of intermediate energy levels within the forbidden band gap. Therefore, the structural distortions on these clusters enhances the formation of e'-$h^{\bullet}$ pairs with concomitant redistribution of the electron density.

In order to further explain the photocatalytic properties of Ag_3PO_4:Mo microcrystals, a model based on Kröger-Vink notation [29] was employed as follows:

$$[AgO_4]^x + [AgO_3V_O^x] \rightarrow [AgO_4]' + [AgO_3V_O^{\bullet}] \quad (3)$$

$$[AgO_4]^x + [AgO_3V_O^{\cdot}] \rightarrow [AgO_4]' + [AgO_3V_O^{\cdot\cdot}] \quad (4)$$

The $[AgO_3V_O^{\cdot}]$ clusters could interact with adsorbed water and separate it into hydroxyl radicals (OH^*) and protons ($H^{\bullet}$), reactive species. Furthermore, the $[AgO_4]'$ $[AgO_4]'_O$ clusters could interact with O_2 molecules, generating superoxide ions (O_2'). Therefore, these species reacted with $H^{\bullet}$ (an unstable species) and formed superoxide radicals (O_2H^*) according to the following equations:

$$[AgO_3V_O^{\bullet}] + H_2O \rightarrow [AgO_3V_O^x] + OH^* + H^{\bullet} \quad (5)$$

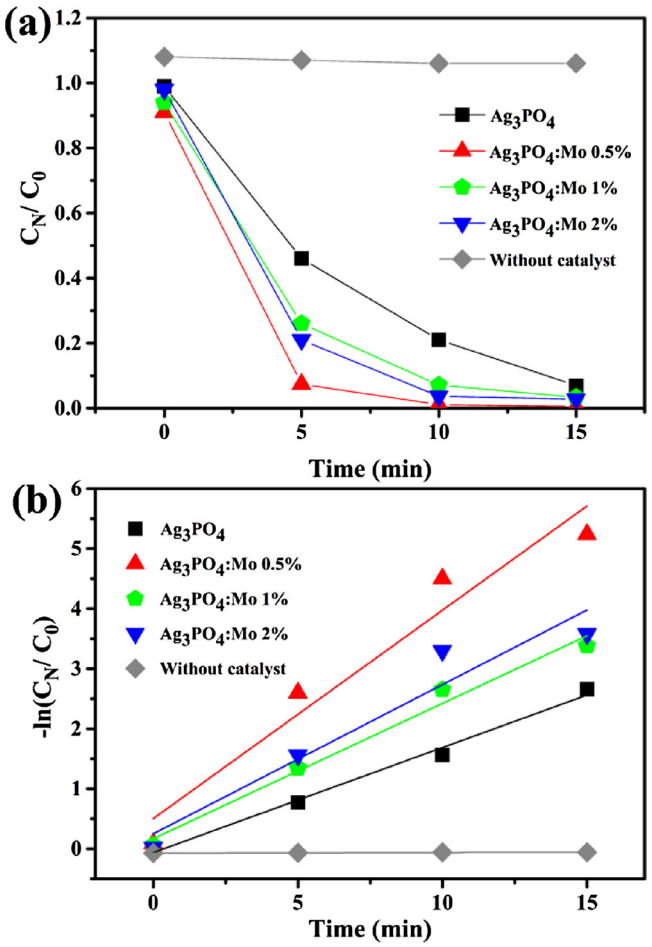

Fig. 12. Photocatalytic degradation of RhB (1.0×10^{-5} mol L^{-1}) in the absence and in the presence of Ag_3PO_4 and Ag_3PO_4 doped with different amounts of Mo in linear plot **(a)** and in log plot for the determination of the rate constant **(b)**.

Table 5
Pseudo-first-order rate constants (k') using Langmuir-Hinshelwood kinetics, for Ag_3PO_4 and Ag_3PO_4 with different amounts of Mo.

Parameters	Ag_3PO_4	Ag_3PO_4 :Mo 0.5%	Ag_3PO_4. Mo 1%	Ag_3PO_4 :Mo 2%	Without Catalyst
k' (min^{-1})	0.175	0.347	0.225	0.248	9.6×10^{-4}

$$[AgO_4]^{'} + O_2 \rightarrow [AgO_4]^{x} + O_2^{'} \quad (6)$$

$$O_2^{'} + H^{\bullet} \rightarrow O_2H^{*} \quad (7)$$

The next step was the RhB photodegradation using these oxidant species (O_2H^* and OH^*) formed under visible light irradiation (5 min for Ag_3PO_4:Mo 0.5%), according to the following equation:

$$RhB \xrightarrow{O_2H^{*}+OH^{*}} CCO + CO_2 + H_2O \quad (8)$$

where CCO refer to colorless organic compounds.

For the Ag_3PO_4:Mo microcrystals, the $[MoO_4]^{\bullet}$ clusters were also involved in the photocatalytic mechanism, *i.e.*, a lower Mo-doping concentration improved the degradation rate, whereas a higher concentration decreased the photocatalytic power. This could be explained by the interaction between the $[AgO_3V_O^{\bullet}]$ and $[MoO_4]^{\bullet}$ clusters, according to equation below:

$$[AgO_3V_O^{\bullet}] + [MoO_4]^{\bullet} \rightarrow [AgO_3V_O^{\cdot}] + [MoO_4]^{x} \quad (9)$$

This cluster-cluster interaction presents two important roles. First, $[MoO_4]^x$ clusters (Equation 9) are formed. They also enhanced the formation of O_2', which in turn, was one of the dominant species as part of the mechanisms responsible for the photocatalytic activity.

$$[MoO_4]^{x} + O_2 \rightarrow [MoO_4]^{\bullet} + O_2^{'} \quad (10)$$

Hence, the $[AgO_4]^{'}$ and $[AgO_3V_O^{\cdot}]$ clusters are responsible for degradation in pure and doped samples. However, in doped samples we also have $[MoO_4]^{\bullet}$ defective clusters, which have a double role on the degradation (Equation 9): 1) when in low concentration (0.5% sample), they generate $[MoO_4]^x$ clusters by interacting with $[AgO_3V_O^{\cdot}]$. The $[MoO_4]^x$ previously formed interacts with O_2 and increases the degradation rate. 2) in high concentration of Mo (1% and 2%), more $[AgO_3V_O^{\cdot}]$ clusters are formed, decreasing the concentration of the $[AgO_3V_O^{\cdot}]$ clusters by this same Equation 9. Since the $[AgO_3V_O^{\cdot}]$ clusters did not interact with water due to the presence of paired electrons, the production of protons ($H\cdot$) decreased and in turn, the production of superoxide radicals (O_2H^*) also decreased, suppressing the degradation. Hence, the role of Mo is a thin line in photocatalytic activity of the samples; it can induce change in the density and kind of defects into the structure. In this way, the small doping was able to create more defects active for RhB degradation than the high doping. These vacancies (deep defects) served as traps, delaying the recombination of charge carriers and consequently greater photocatalytic activity. Thus, the Mo-dopant could increase the photocatalytic power, but could also inhibit photocatalysis depending on its concentration in the lattice.

After understanding how the photocatalytic mechanism occurs in the Ag_3PO_4:Mo 0.5%, it is possible to explain why the lower activity observed in the Ag_3PO_4. In the scavengers results were observed that the OH^* species are important in the photocatalytic mechanism and the lower activity suggest that there are another reaction occurring in the processes, prevent the OH^* participation on the processes (Equation 11).

$$4OH^{*} \rightarrow O_2 + 2H_2O \quad (11)$$

According to Equations 8 and 11, the decreases of OH^* concentration provokes a lower percentage of degradation for the Ag_3PO_4. In summary, the photocatalytic mechanisms for Ag_3PO_4 and Ag_3PO_4:Mo 0.5% involves the presence of OH*, O_2', O_2H^* and $H\cdot$, and the molecular mechanism is controlled by a subtle and complex equilibrium of these reactive species along the above equations.

4. Conclusions

In summary, new Ag_3PO_4:Mo based photocatalysts were obtained using a simple, eco-friendly and easily scalable CP route. Subsequently the photocatalysts were fully characterized. Analysis of the XRD patterns rendered that the samples were single-phased up to a 2% substitution of P(V) by Mo(VI) cations. The actual substitution inside the Ag_3PO_4 crystalline network was further confirmed by micro-Raman, XPS, UV–vis absorption, and PL spectra. The HR-TEM maps did not evidence any segregation of the Mo(VI) cation inside the analyzed microcrystals. Theoretical calculations allowed us to explain and rationalize present experimental results.

The insertion of Mo as dopant into the crystalline network of the Ag_3PO_4 structure caused impurities and local defects, decreasing the band gap due to the formation of new intermediate levels between the VB and CB, as seen from the results of PL emissions as well as from theoretical calculations. These associated levels created in the gap would improve the photocatalytic performance of the material, since these defects in the structure generated active sites. The photocatalytic experiments, probed by the discoloration of RhB, were carried out under visible light irradiation. It appeared that the most efficient material was the 0.5% Mo-doped sample, which degraded the dye two times faster than the pure Ag_3PO_4 microcrystals, and was a little bit more stable under cycling. The photocatalytic mechanism for

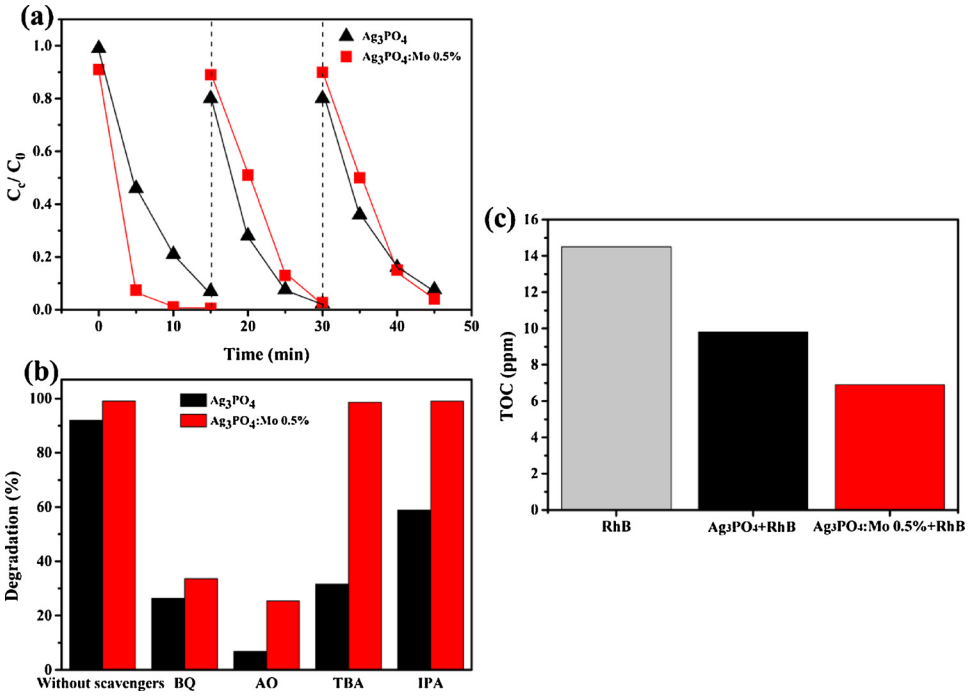

Fig. 13. Influence of various scavengers onto the photocatalytic degradation of RhB in the presence ofAg_3PO_4:Mo 0.5% catalyst **(a)**, cycling runs for RhB photodegradation over pure Ag_3PO_4 and Ag_3PO_4:Mo 0.5% under visible light irradiation. For second and third cycles no equilibrium time in the dark was applied **(b)** and decreased TOC of rhodamine B solution in presence of Ag_3PO_4 and Ag_3PO_4: Mo 0.5% over a period of 30 min of under visible light irradiation **(c)**.

theAg_3PO_4:Mo microcrystals was dominated by the presence of superoxide radicals and oxygen vacancies. Consequently, the presence of the Mo clusters had an important role in the mechanism.

This study provides a class of Ag_3PO_4:Mo photocatalysts operating more efficiently under visible light compared to previous ones like TiO_2, which is only active under UV irradiation. Moreover, their good stability and easy synthesis under soft conditions give them a special importance in the actual challenge for pollutant elimination, energy saving, and earth preservation.

This experimental and theoretical work provides insights into the fine effects controlling the correlation among structural, optical, and electronic properties and photocatalytic activity of Ag_3PO_4:Mo. The results have been discussed by a conciliation and association of the results acquired by experimental procedures and first-principles calculations.

Acknowledgements

This work was financially supported by Fundação de Amparo à Pesquisa do Estado de São Paulo (FAPESP 2013/07296-2 and 2013/26671-9) and Coordenação de Aperfeiçoamento de Pessoal de Nível Superior (CAPES/PNPD). J. A. and M. O. acknowledge the financial support from: Universitat Jaume I, project UJI-B2016-25, Generalitat Valenciana project Prometeo/2016/079, Ministerio de Economia y Competitividad, project CTQ2015-65207-P. TOC facilities were provided by LaPE (Laboratório de Pesquisas em Eletroquímica). The authors wish to acknowledge Isaac J. S. Montes (UFSCar) and Prof. Dr. José M. de Aquino (UFSCar) for their generous help with the TOC analysis. The authors would especially like to express gratitude to Prof. Dr. Edson R. Leite (UFSCar/CNPEM) for stimulating scientific discussions and help in the TEM operation.

Appendix A. Supplementary data

Supplementary material related to this article can be found, in the online version, at doi:https://doi.org/10.1016/j.apcatb.2018.07.019.

References

[1] T.J. Yan, W.F. Guan, J. Tian, P. Wang, W.J. Li, J.M. You, B.B. Huang, J. Alloys Compd. 680 (2016) 436–445.
[2] Z.G. Yi, J.H. Ye, N. Kikugawa, T. Kako, S.X. Ouyang, H. Stuart-Williams, H. Yang, J.Y. Cao, W.J. Luo, Z.S. Li, Y. Liu, R.L. Withers, Nat. Mater. 9 (2010) 559–564.
[3] Y.Z. Ma, F. Cheng, W.S. Liu, J. Wang, Y.K. Wang, Trans. Nonferrous Met. Soc. China 25 (2015) 112–121.
[4] J.-K. Liu, C.-X. Luo, J.-D. Wang, X.-H. Yang, X.-H. Zhong, CrystEngComm 14 (2012) 8714–8721.
[5] G. Panthi, R. Ranjit, H.-Y. Kim, D.D. Mulmi, Optik – Int. J. Light Electron Optics 156 (2018) 60–68.
[6] X.J. Chen, Y.Z. Dai, X.Y. Wang, J. Alloys Compd. 649 (2015) 910–932.
[7] Y.H. Song, H.Z. Zhao, Z.G. Chen, W.R. Wang, L.Y. Huang, H. Xu, H.M. Li, Phys, Status Solidi A 213 (2016) 2356–2363.
[8] X. Yang, H. Tang, J. Xu, M. Antonietti, M. Shalom, ChemSusChem 8 (2015) 1350–1358.
[9] H. Tang, Y. Fu, S. Chang, S. Xie, G. Tang, Chin. J. Catal. 38 (2017) 337–347.
[10] W.R. Cao, Y.T. An, L.F. Chen, Z.W. Qi, J. Alloys Compd. 701 (2017) 350–357.
[11] G. Botelho, J.C. Sczancoski, J. Andres, L. Gracia, E. Longo, J. Phys. Chem. C 119 (2015) 6293–6306.
[12] G. Botelho, J. Andres, L. Gracia, L.S. Matos, E. Longo, ChemPhysChem 81 (2016) 202–212.
[13] K. Maeda, K. Domen, J. Phys. Chem. Lett. 1 (2010) 2655–2661.
[14] R. Konta, T. Ishii, H. Kato, A. Kudo, J. Phys. Chem. B 108 (2004) 8992–8995.
[15] M. Miyauchi, M. Takashio, H. Tobimatsu, Langmuir 20 (2004) 232–236.
[16] S.W. Bae, P.H. Borse, J.S. Lee, Appl. Phys. Lett. (2008) 92.
[17] M.S.A. Hussien, I.S. Yahia, J. Photochem. Photobiol. A 356 (2018) 587–594.
[18] R. Dovesi, V.R. Saunders, C. Roetti, R. Orlando, C.M. Zicovich-Wilson, F. Pascale, B. Civalleri, K. Doll, N.M. Harrison, I.J. Bush, P. D'Arco, M. Llunel, M. Causà, Y. Noël, CRYSTAL14 User's Manual, Theoretical Chemistry Group, University of Turin, Italy, 2014.
[19] R. Dovesi, R. Orlando, A. Erba, C.M. Zicovich-Wilson, B. Civalleri, S. Casassa, L. Maschio, M. Ferrabone, M. De La Pierre, P. D'Arco, Y. Noel, M. Causa, M. Rerat, B. Kirtman, Int. J. Quantum Chem. 114 (2014) 1287–1317.
[20] A.D. Becke, J. Chem. Phys. 98 (1993) 5648–5652.
[21] C.T. Lee, W.T. Yang, R.G. Parr, Phys. Rev. B: Condens. Matter Mater. Phys. 37 (1988) 785–789.
[22] Crystal, http://www.crystal.unito.it/Basis_Sets/Ptable.html.
[23] D.P. Rai, A. Shankar, Sandeep, M.P. Ghimire, R. Khenata, R.K. Thapa, RSC Adv. 5 (2015) 95353–95359.
[24] D.P. Rai, A. Laref, A. Shankar, Sandeep, A.P. Sakhya, R. Khenata, R.K. Thapa, J. Phys. Chem. Solids 120 (2018) 104–108.
[25] L. Helmholz, J. Chem. Phys. 4 (1936) 316–322.
[26] R. Masse, I. Tordjman, A. Durif, Z. Kristallogr. 144 (1976) 76–81.
[27] H.N. Ng, C. Calvo, R. Faggiani, Acta Crystallogr, Sect. B: Struct. Sci. 34 (1978) 898–899.
[28] M.N. Deschizeauxcheruy, J.J. Aubert, J.C. Joubert, J.J. Capponi, H. Vincent, Solid State Ionics 7 (1982) 171–176.
[29] F.A. Kröger, H.J. Vink, Solid State Phys. 3 (1956) 307–435.
[30] N.A. Zarkevich, T.L. Tan, D.D. Johnson, Phys, Rev. B 75 (2007) 104203.

[31] M. Mroczkowska, J.L. Nowinski, G.Z. Zukowska, A. Mroczkowska, J.E. Garbarczyk, M. Wasiucionek, S. Gierlotka, J. Power Sources 173 (2007) 729–733.
[32] P.Y. Dong, Y.H. Wang, B.C. Cao, S.Y. Xin, L.N. Guo, J. Zhang, F.H. Li, Appl. Catal., B 132 (2013) 45–53.
[33] M.T. Fabbro, C.C. Foggi, L.P.S. Santos, L. Gracia, A. Perrin, C. Perrin, C.E. Vergani, A.L. Machado, J. Andres, E. Cordoncillo, E. Longo, Dalton Trans. 45 (2016) 10736–10743.
[34] J. Andres, M.M. Ferrer, L. Gracia, A. Beltran, V.M. Longo, G.H. Cruvinel, R.L. Tranquilin, E. Longo, Part. Part. Syst. Charact. 32 (2015) 646–651.
[35] A.F. Gouveia, J.C. Sczancoski, M.M. Ferrer, A.S. Lima, M.R. Santos, M.S. Li, R.S. Santos, E. Longo, L.S. Cavalcante, Inorg. Chem. 53 (2014) 5589–5599.
[36] J.V. Kumar, R. Karthik, S.M. Chen, V. Muthuraj, C. Karuppiah, Sci. Rep. 6 (2016).
[37] H. Zhang, G. Wang, D. Chen, X.J. Lv, U.H. Jinghong, Chem. Mater. 20 (2008) 6543–6549.
[38] Y.P. Liu, L. Fang, H.D. Lu, Y.W. Li, C.Z. Hu, H.G. Yu, Appl. Catal. B 115 (2012) 245–252.
[39] C.X. Zhang, K. Yu, Y.J. Feng, Y. Chang, T. Yang, Y. Xuan, D. Lei, L.L. Lou, S.X. Liu, Appl. Catal. B 210 (2017) 77–87.
[40] Y. Chang, M.L. Lye, H.C. Zeng, Langmuir 21 (2005) 3746–3748.
[41] S. Kaciulis, G. Mattogno, L. Pandolfi, M. Cavalli, G. Gnappi, A. Montenero, Appl. Surf. Sci. 151 (1999) 1–5.
[42] Z.H. Chen, F. Bing, Q. Liu, Z.G. Zhang, X.M. Fang, J. Mater. Chem. A 3 (2015) 4652–4658.
[43] H. Katsumata, T. Sakai, T. Suzuki, S. Kaneco, Ind. Eng. Chem. Res. 53 (2014) 8018–8025.
[44] Y.F. Li, Y.J. Hu, J.H. Shen, H.B. Jiang, G.Q. Min, S.J. Qiu, Z.T. Song, Z. Sun, C.Z. Li, Nanoscale 7 (2015) 18603–18611.
[45] J.J. Zhang, T. Huang, L.J. Zhang, A.S. Yu, J. Mater. Chem. C 118 (2014) 25300–25309.
[46] G.S. Silva, L. Gracia, M.T. Fabbro, L.P. Serejo dos Santos, H. Beltrán-Mir, E. Cordoncillo, E. Longo, J. Andrés, Inorg. Chem. 55 (2016) 8961–8970.
[47] N.G. Macedo, A.F. Gouveia, R.A. Roca, M. Assis, L. Gracia, J. Andrés, E.R. Leite, E. Longo, J. Phys. Chem. C 122 (2018) 8667–8679.
[48] E. Longo, L.S. Cavalcante, D.P. Volanti, A.F. Gouveia, V.M. Longo, J.A. Varela, M.O. Orlandi, J. Andres, Sci. Rep. 3 (2013) 1676.
[49] J. Andres, L. Gracia, P. Gonzalez-Navarrete, V.M. Longo, W. Avansi Jr., D.P. Volanti, M.M. Ferrer, P.S. Lemos, F.A. La Porta, A.C. Hernandes, E. Longo, Sci. Rep. 4 (2014) 5391–5397.
[50] E. Longo, D.P. Volanti, V.M. Longo, L. Gracia, I.C. Nogueira, M.A.P. Almeida, A.N. Pinheiro, M.M. Ferrer, L.S. Cavalcante, J. Andres, J. Phys. Chem. C 118 (2014) 1229–1239.
[51] V.M. Longo, C.C. De Foggi, M.M. Ferrer, A.F. Gouveia, R.S. Andre, W. Avansi, C.E. Vergani, A.L. Machado, J. Andres, L.S. Cavalcante, A.C. Hernandes, E. Longo, J. Phys. Chem. A 118 (2014) 5769–5778.
[52] E.R. Jette, F. Foote, J. Chem. Phys. 3 (1935) 605–616.
[53] L. Tolvaj, K. Mitsui, D. Varga, Wood Sci. Technol. 45 (2011) 135–146.
[54] Q.Y. Lu, K.L. Chen, W. Pan, X.W. Wu, K.D. Lu, Z.D. Xu, R. Liu, J. Electrochem. Soc. 163 (2016) D206–D211.
[55] X. Ma, B. Lu, D. Li, R. Shi, C. Pan, Y. Zhu, J. Phys. Chem. C 115 (2011) 4680–4687.
[56] J.M. Kahk, D.L. Sheridan, A.B. Kehoe, D.O. Scanlon, B.J. Morgan, G.W. Watson, D.J. Payne, J. Mater. Chem. A 2 (2014) 6092–6099.
[57] C.W. Raubach, A.F. Gouveia, Y.V.B. de Santana, J.A. Varela, M.M. Ferrer, M.S. Li, E. Longo, J. Mater. Chem. C 2 (2014) 2743–2750.
[58] Y.V.B. De Santana, J.E.C. Gomes, L. Matos, G.H. Cruvinel, A. Perrin, C. Perrin, J. Andres, J.A. Varela, E. Longo, Nanomater. Nanotechnol. 4 (2014) 22–31.
[59] N. Guettai, H.A. Amar, Desalination 185 (2005) 439–448.
[60] K. Huang, Y. Lv, W. Zhang, S. Sun, B. Yang, F. Chi, S. Ran, X. Liu, Mater. Res. 18 (2015) 939–945.
[61] J.J. Liu, X.L. Fu, S.F. Chen, Y.F. Zhu, Appl. Phys. Lett. 99 (2011) 191903.
[62] N. Umezawa, O. Shuxin, J. Ye, Phys. Rev. B 83 (2011) 035202.
[63] W.G. Wang, B. Cheng, J.G. Yu, G. Liu, W.H. Fan, Chem, Asian J. 7 (2012) 1902–1908.
[64] J.F. Ma, Q. Liu, L.F. Zhu, J. Zou, K. Wang, M.R. Yang, S. Komarneni, Appl. Catal., B 182 (2016) 26–32.
[65] X.Q. Liu, W.J. Chen, H. Jiang, Chem. Eng. J. 308 (2017) 889–896.
[66] J. Ren, Y.Y. Chai, Q.Q. Liu, L. Zhang, W.L. Dai, Appl. Surf. Sci. 403 (2017) 177–186.
[67] Y.L. Zhang, C.R. Xie, F.L. Gu, H.H. Wu, Q. Guo, J. Hazard. Mater. 315 (2016) 23–34.